Influence of ionosphere conductivity on the ring current

Y. Ebihara,[1] M.-C. Fok,[2] R. A. Wolf,[3] T. J. Immel,[4] and T. E. Moore[2]

Received 6 December 2003; revised 21 April 2004; accepted 29 April 2004; published 28 August 2004.

[1] Using the Comprehensive Ring Current Model (CRCM), which self-consistently solves the kinetic equation of ring current protons and the closure of the electric current between the magnetosphere and ionosphere, we have studied how different changes in the ionospheric conductivity affect the strength of the ring current. The conductivity for F10.7 = 250 $\times$ 10^4 Janskys (Jy) (solar maximum condition) results in a ring current that is about 29% stronger than for F10.7 = 70 $\times$ 10^4 Jy (solar minimum condition). The conductivity at equinox results in a ring current that is about 5% stronger than at solstice because the two-hemisphere height-integrated conductivities at equinox are higher than at solstice. This would be a new mechanism for explaining the semiannual variation of *Dst*. Simulation with a realistic auroral conductivity estimated from the Imager for Magnetopause-to-Aurora Global Exploration (IMAGE)/Far Ultraviolet Imager (FUV) auroral imager data reveals the fact that auroral brightenings do not significantly change the intensity of the ring current. The overshielding condition is found to be produced when the auroral conductivity decreases abruptly near the *Dst* minimum, triggering a rapid decay of the ring current. The ring current is shown to be influenced not only by the interplanetary magnetic field and the solar wind but also by solar radiation and morphological features of the auroral electron precipitation as well. *INDEX TERMS:* 2778 Magnetospheric Physics: Ring current; 2736 Magnetospheric Physics: Magnetosphere/ionosphere interactions; 2730 Magnetospheric Physics: Magnetosphere—inner; 2720 Magnetospheric Physics: Energetic particles, trapped; *KEYWORDS:* magnetic storms, ring current, ionosphere conductivity, sheilding, *Dst* index, numerical simulation

Citation: Ebihara, Y., M.-C. Fok, R. A. Wolf, T. J. Immel, and T. E. Moore (2004), Influence of ionosphere conductivity on the ring current, *J. Geophys. Res.*, *109*, A08205, doi:10.1029/2003JA010351.

1. Introduction

[2] Earth's ionosphere is filled with dense thermal plasma as a consequence of ionization of atmospheric constituents by solar EUV radiation and precipitation of energetic particles. With regard to the ring current development, the ionosphere is thought to be (1) a supplier of plasma to the ring current and (2) a conducting layer that electrically couples with the magnetosphere.

[3] The role of the ionosphere as a source of the ring current particles is clearly identified by satellite-borne instruments that measure singly charged oxygen ions or nitrogen ions [*Lundin et al.*, 1980; *Gloeckler et al.*, 1985; *Hamilton et al.*, 1988; *Moore and Delcourt*, 1995; *Roeder et al.*, 1996; *Daglis*, 1997; *Christon et al.*, 2002; *Mall et al.*, 2002]. Since the singly charged oxygen ions or nitrogen ions are extremely rare in the solar wind, they are good tracers of particles originating from the ionosphere.

[4] The effect of the ionosphere as a conducting layer has not clearly been identified in terms of the degree of its influence on the ring current development. The reason is that the coupling process between the ionosphere and the magnetosphere is essentially nonlinear. Numerical simulation under realistic conditions seems to be the most appropriate way to understand the role of the ionosphere in ring current development, especially during storms.

[5] *Vasyliunas* [1970] proposed a self-consistent model that takes into account the current closure between the ring current and the ionosphere. In this model the field-aligned current is produced by a longitudinal gradient of the plasma pressure in the magnetosphere. Then, given an appropriate model of the ionospheric conductance, the ionospheric electric potential is calculated from the requirement that the ionosphere conducts away the charge deposited by the field-aligned currents. This results in a shielding electric field. This updated electric potential is mapped to the magnetosphere along magnetic field lines, and motion of particles in the magnetosphere is modified by the updated electric field.

[6] R. Wolf and his coworkers developed a computer code called the Rice Convection Model to solve the self-consistent model numerically (see *Wolf* [1970], *Jaggi and Wolf* [1973], *Harel et al.* [1981a, 1981b], *Spiro et al.* [1981], *Wolf et al.* [1982], *Spiro and Wolf* [1984], and *Toffoletto et al.* [2003] for review). *Wolf* [1970] first investigated effects

[1]Universities Space Research Association, NASA Goddard Space Flight Center, Greenbelt, Maryland, USA.
[2]NASA Goddard Space Flight Center, Greenbelt, Maryland, USA.
[3]Rice University, Houston, Texas, USA.
[4]University of California, Berkeley, California, USA.

0148-0227/04/2003JA010351

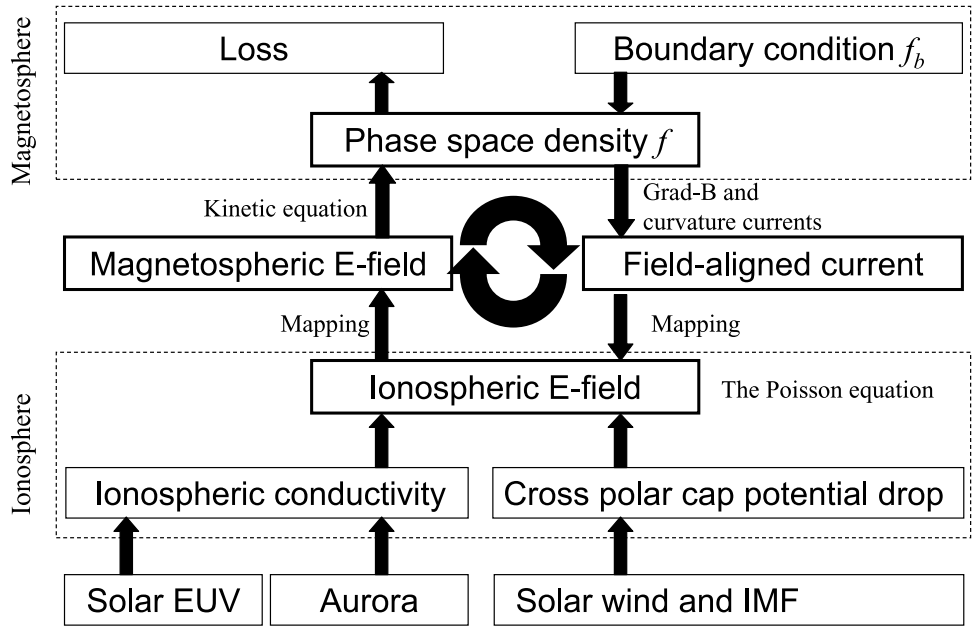

Figure 1. Block diagram of the CRCM. We investigated the influence of the ring current on the ionospheric conductivity in terms of the solar EUV and the auroral electron precipitation.

of the ionospheric conductivity on the global distribution of electric fields and currents and obtained drift trajectories of magnetospheric particles. *Spiro and Wolf* [1984] found that the total energy of the ring current increases by a factor of 1.4 when the ionospheric conductivity is doubled. Increased conductivity results in the decreased shielding that allows particles to drift further into the inner magnetosphere. *Senior and Blanc* [1984] developed a self-consistent model including spatial variations of the ionospheric conductivity. A linear approximation of the motion of the ring current inner edge was used in their calculation. They showed that auroral enhancement of the ionospheric conductivity increases the shielding time constant and that the midlatitude electric field is attenuated by a factor of about 3 or 4 by the shielding mechanism.

[7] After the development of the RCM and *Senior and Blanc*'s [1984] models, many numerical simulations of the ring current have been performed (e.g., *Chen et al.* [1993], *Fok et al.* [1995], *Jordanova et al.* [1996], *Ebihara and Ejiri* [1998], *Liemohn et al.* [1999], and *Ebihara and Ejiri* [2003] for review). The simulations employing an empirical model of the convection electric field (e.g., Volland-Stern [*Volland*, 1973; *Stern*, 1975] or the Weimer model [*Weimer*, 1995, 2001]) provide a reasonable result regarding the ion distribution, the pressure, and *Dst*. Such a non-self-consistent simulation takes into account the shielding effect because such empirical models of the convection electric field include a mathematical expression of the shielding effect implicitly.

[8] *Fok et al.* [2001] developed a hybrid simulation scheme called the Comprehensive Ring Current Model (CRCM). The kinetic equation of particles is calculated by Fok's ring current model [*Fok et al.*, 1995; *Fok and Moore*, 1997], and the closure of the electric current is calculated by the RCM [*Toffoletto et al.*, 2003].

[9] *Ridley and Liemohn* [2002] calculated the pattern of the shielding electric field driven by the ring current. Recently, *Khazanov et al.* [2003] improved *Ridley and Liemohn*'s [2002] computer code and performed a self-consistent simulation that calculates the electric coupling between the magnetosphere and the ionosphere. A dipole magnetic field was used in their calculations [*Ridley and Liemohn*, 2002; *Khazanov et al.*, 2003], while the CRCM is capable of solving the equations with a realistic magnetic field model [*Fok et al.*, 2001].

[10] The purpose of this paper is to investigate the role of the ionospheric conductivity in the development of the ring current, especially during the storm main phase. In particular, we focus on changes in ionospheric conductance due to the solar radiation, tilt angle, and precipitating electrons. This paper consists of seven sections. After describing our simulation scheme in section 2, results of a "reference run" are shown in section 3. In section 4 the influence of the solar activity on the ring current is studied by simulations carried out for various values of the F10.7 index. In section 5 the influence of the tilt angle is studied on the basis of simulations performed for various tilt angles in terms of day of year. Section 6 presents results for various assumed auroral conductivity models. Section 7 summarizes the results.

2. Simulation

[11] The following is a brief description of the CRCM and the initial and boundary conditions that were used in this particular study. The numerical scheme is described in detail by *Fok et al.* [2001] and is schematically drawn in Figure 1.

2.1. Kinetic Equation

[12] Neglecting the gyrophase and the bounce phase of charged particles, we specified particles in terms of a four-

dimensional phase space, two-dimensional position, and two adiabatic invariants M and K, which are

$$M = \frac{p^2 \sin^2 \alpha}{2m_0 B}, \tag{1}$$

$$K = \int_{sm_1}^{sm_2} \sqrt{B_m - B(s)}\, ds, \tag{2}$$

where p is the momentum, α is the pitch angle, m_0 is the rest mass, B is the magnetic field, and B_m is the magnetic field at the mirror points sm_1 and sm_2.

[13] The spatial and temporal variation of the phase space density of charged particles is obtained by solving the bounce-averaged Boltzmann equation, that is,

$$\frac{\partial \overline{f}_s}{\partial t} + \langle \dot{l}_i \rangle \frac{\partial \overline{f}_s}{\partial l_i} + \left\langle \dot{\phi}_i \right\rangle \frac{\partial \overline{f}_s}{\partial \phi_i} = -v\sigma_s \langle n_H \rangle \overline{f}_s - \left(\frac{\overline{f}_s}{0.5\tau_b} \right)_{\text{loss cone}}, \tag{3}$$

where $\overline{f}_s = \overline{f}_s(l_i, \phi_i, M, K)$ is the four-dimensional phase space density, l_i is the magnetic latitude at ionospheric altitude (r_i), ϕ_i is the magnetic local time at the ionospheric altitude, v is the velocity of particle, σ_H is the cross section for charge exchange, n_H is the hydrogen density, and τ_b is the bounce period. The operator $\langle\rangle$ indicates a bounce average over a field line between two mirror points sm_1 and sm_2. The atmospheric absorption altitude for the loss cone is defined as 100 km.

[14] The bounce-averaged drift velocities, $\langle \dot{l}_i \rangle$ and $\langle \dot{\phi}_i \rangle$, are expressed [*Fok and Moore*, 1997] as

$$\langle \dot{l}_i \rangle = -\frac{1}{qG} \frac{\partial H}{\partial \phi_i}, \tag{4}$$

$$\langle \dot{\phi}_i \rangle = \frac{1}{qG} \frac{\partial H}{\partial l_i}, \tag{5}$$

where $G = M_E \sin(2l_i)/r_i$ and M_E is the Earth's magnetic dipole moment. The Hamiltonian H is given by

$$H = W + q\Phi - \frac{q\Omega M_E}{2r_i} \cos 2l_i, \tag{6}$$

where q is the charge, Φ is the electric potential, and Ω is the angular velocity of the rotation of the Earth. The right-hand side of equation (6) represents magnetic drift (the grad-B and curvature drifts), the $\mathbf{E} \times \mathbf{B}$ drift by the convection electric field, and the $\mathbf{E} \times \mathbf{B}$ drift by the corotation electric field, respectively. The above formulation enables tracking motion of particles with an arbitrary equatorial pitch angle in a nondipolar magnetic field.

2.2. Field-Aligned Current and Ionospheric Electric Potential

[15] The RCM algorithm was used to calculate the field-aligned current and the ionospheric electric potential. We converted the phase space density $\overline{f}_s(l_i, \phi_i, M, K)$ to $\eta(l_i, \phi_i, M, K)$, that is, the number of particles per unit magnetic flux in the ranges $(M, M + \Delta M)$, $(K, K + \Delta K)$, using the formula

$$\eta = 4\sqrt{2}\pi m_0^{3/2} \overline{f} M^{1/2} \Delta M \Delta K. \tag{7}$$

[16] The field-aligned current is then given by

$$\frac{J_{\|i}}{B_i} = \sum_j \frac{\mathbf{B}}{B^2} \cdot \left(\nabla \eta_j \times \nabla W_j \right), \tag{8}$$

which can be rewritten as

$$J_{\|i} = \frac{1}{r_i^2 \cos l_i} \sum_j \left(\frac{\partial \eta_j}{\partial l_i} \frac{\partial W_j}{\partial \phi_i} - \frac{\partial \eta_j}{\partial \phi_i} \frac{\partial W_j}{\partial l_i} \right). \tag{9}$$

(positive downward)

The ionospheric potential Φ_i is given by solving the Poisson equation as

$$\nabla \cdot (-\Sigma \cdot \nabla \Phi_i) = J_{\|i} \sin I, \tag{10}$$

where Σ is a tensor of height-integrated conductance and I is the magnetic dip angle.

[17] Contributions from both northern and southern hemispheres are taken into consideration in calculation of the conductance tensor Σ because a line integral between foot points in the northern and southern hemispheres is performed in the derivation of equation (8). Assuming that the ionospheric conductance produced by incident energetic particles is the same in the two hemispheres, the two-hemisphere conductivity Σ is given by

$$\Sigma = 2\Sigma_{\text{precipitation}} + \Sigma_{\text{background, northern hemisphere}} + \Sigma_{\text{background, southern hemisphere}}. \tag{11}$$

The International Reference Ionosphere (IRI-95) [*Bilitza*, 1997] and the Mass Spectrometer Incoherent Scatter (MSIS-E90) model [*Hedin*, 1991] were employed to calculate the background conductance. The IRI-95 model requires day of year and the F10.7 index, and the MSIS-90E model requires day of year, the F10.7 index, and the Ap index as input parameters. The difference between the local time and the geographical longitude is not taken into account; that is, the universal time (UT) dependence of the conductivity is not included. *Hardy et al.* [1985] compiled DMSP measurements of precipitating electrons and provided an empirical model of them as a function of magnetic local time, magnetic latitude and Kp. We used the empirical model of *Hardy et al.* [1987], who calculated the Hall and Pedersen conductivities for different Kp levels based on the empirical model of precipitating electron energy flux and average energy, by using the formulae of *Robinson et al.* [1987].

[18] The cross polar cap potential drop Φ_P was given by an empirical model of *Boyle et al.* [1997], who obtained a mathematical expression between Φ_P and the solar wind velocity and interplanetary magnetic field (IMF) as

$$\Phi_P = 1.1 \times 10^{-4} V_{sw}^2 + 11.1 B_{\text{IMF}} \sin^3 \left(\frac{\theta_{\text{IMF}}}{2} \right) \text{ (kV)}, \tag{12}$$

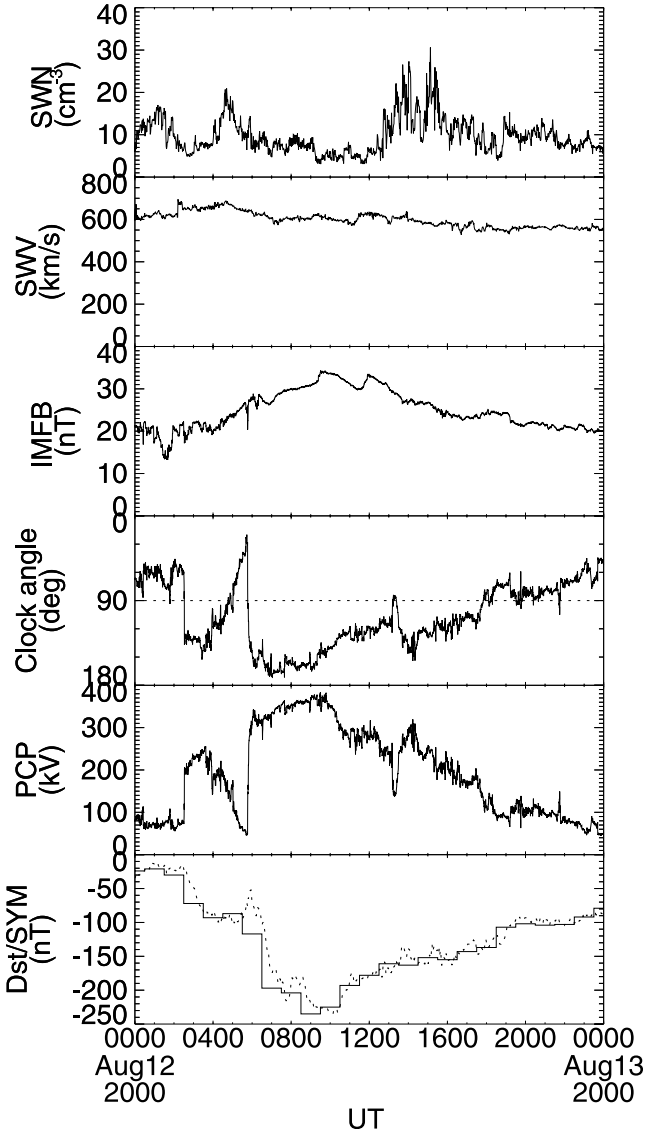

Figure 2. Interplanetary and geomagnetic quantities during the storm of 12 August 2000. From top to bottom are the solar wind density, the solar wind velocity, the intensity of IMF, the clock angle of IMF (positive northward), the polar cap potential drop calculated by the formula of *Boyle et al.* [1997], and *Dst* (solid) and SYM (dashed) indices.

where V_{sw} is the solar wind velocity in km/s, B_{IMF} is the magnitude of IMF in nT, and θ_{IMF} is the clock angle of IMF. We used IMF and solar wind data from the ACE satellite.

[19] The electric potential calculated by equation (10) was mapped along field lines under the assumption that the field line is equipotential. The newly updated electric field was used to solve the kinetic equation (3).

[20] The outer boundary of the ionosphere for the Poisson equation (10) was located at 66.7deg at 100 km altitude, and the boundary of the magnetosphere for the particle injection was located at the radial distance of 10 *Re* in the equatorial plane. We consider only protons, and the distribution function at the boundary was held constant and assumed to be isotropic Maxwellian with density of 0.5 cm^{-3} and temperature of 5 keV. The magnetosphere was initially filled with preexisting particles with the distribution function measured by AMPTE/CCE in quiet time [*Sheldon and Hamilton*, 1993].

[21] We calculated *Dst** by using the Dessler-Parker-Sckopke relationship [*Dessler and Parker*, 1959; *Sckopke*, 1966], that is,

$$Dst^*(\mathrm{nT}) = -2.495 \times 10^{-14}\epsilon(\mathrm{J}), \tag{13}$$

where ϵ is the total energy of the ring current. *Dst** stands for *Dst* corrected by the solar wind dynamic pressure as

$$Dst^* = Dst - c_1 P_{sw}^{1/2} + c_2, \tag{14}$$

where P_{sw} is the dynamic pressure of the solar wind and c_1 and c_2 are empirical coefficients. We assumed the coefficients c_1 and c_2 to be 0.2 nT/(eV cm^{-3})$^{1/2}$ and 20 nT, respectively [*Gonzalez et al.*, 1994].

3. Reference Run

[22] We particularly focused on the intense magnetic storm that took place on 12 August 2000. Figure 2 shows interplanetary parameters (solar wind and IMF) and geomagnetic (*Dst* and SYM) indices during the storm. The polar cap potential drop Φ_P estimated by using equation (12) exceeded 300 kV, and *Dst* reached its minimum of −235 nT at 0900 UT. We performed the reference run by putting parameters measured during the storm into the ionospheric conductivity model. The daily F10.7 value was 194.3 × 10^4 Jy, and the daily Ap index was 123.

[23] We used the empirical magnetic field model of *Tsyganenko* [1995] and *Tsyganenko and Stern* [1996] (hereinafter referred to T96). The T96 model provides the external magnetic field parameterized by the solar wind dynamic pressure, the *Dst* index, IMF By, and Bz. The parameters were held constant throughout the simulation to highlight the effect of the ionospheric conductivity. On the basis of the observation made at the beginning of the simulation (0000 UT on 12 August 2000), we selected the parameters; the solar wind dynamics pressure is 4.62 nPa, *Dst* is −26 nT, IMF By is 5.0 nT, and IMF Bz is 5.0 nT.

[24] To clearly illuminate the effect of the ionospheric conductance, we only changed the polar cap potential drop and the auroral conductance. The other parameters were held constant throughout the calculation unless otherwise mentioned. Figure 3 shows snapshots of two pressure terms, $P_\perp$ and $P_\parallel$, and the perpendicular current density $J_\perp$ in the equatorial plane, which is given by

$$\mathbf{J}_\perp = \frac{\mathbf{B}}{B^2} \times \left[\nabla P_\perp + (P_\parallel - P_\perp) \frac{(\mathbf{B}\cdot\nabla)\mathbf{B}}{B^2} \right]. \tag{15}$$

[25] An interesting feature is the highly twisted pattern of the convection electric potential marked by black lines (overlayed on the plasma pressure). The twisting feature started to develop on the nightside when the polar cap potential drop increased. The eastern edge of the twisting corresponds to the eastern edge of the high-pressure region, meaning that newly injected particles from the nightside plasma sheet get closest to the Earth and tend to gain their kinetic energy adiabatically in the vicinity of the twisting.

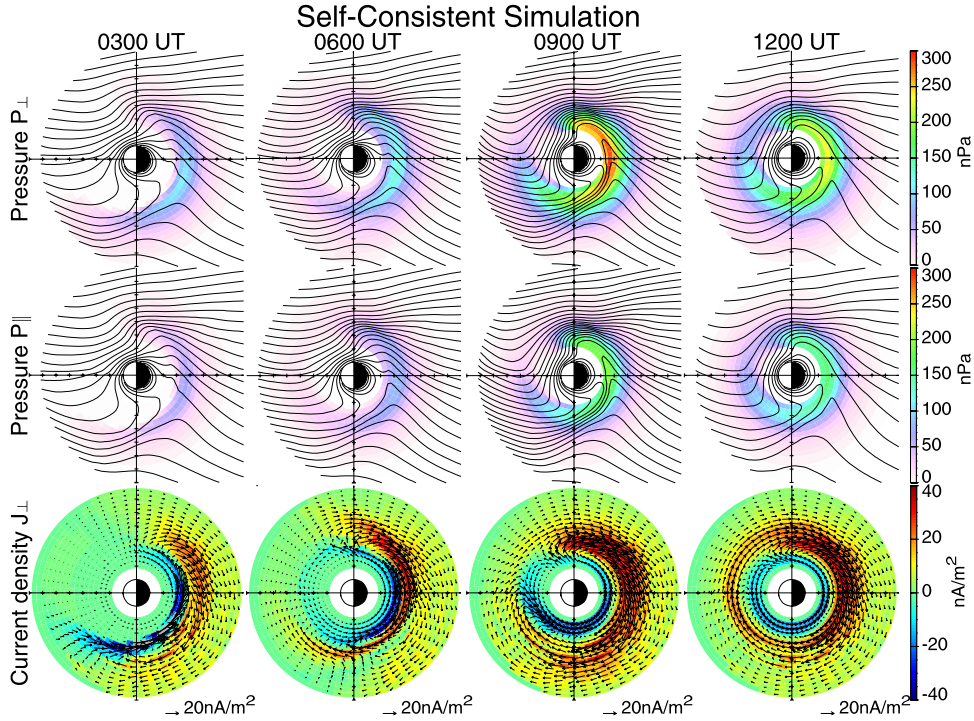

Figure 3. (top) Perpendicular plasma pressure ($P_\perp$), (middle) parallel plasma pressure ($P_\parallel$), and (bottom) perpendicular current density ($J_\perp$) in the equatorial plane for four different times. White lines overlapped with the plasma pressure stand for the equipotential line of convection and corotation electric fields. Current densities flowing eastward (blue) and westward (red) are distinguished by colors. The magnitude and direction of the current density are indicated by an arrow.

Consequently, fluxes of tens-keV-ions peak in the midnight-dawn sector [*Fok et al.*, 2003]. This is consistent with an energetic neutral atom measurement performed by the Imager for Magnetopause-to-Aurora Global Exploration (IMAGE)/High-Energy Neutral Atom (HENA) instrument [*C:son Brandt et al.*, 2002]. In addition, the pressure peak occurs near midnight, which is consistent with the statistically obtained pressure distribution during a storm main phase [*Ebihara et al.*, 2002]. This result contrasts with the result calculated with a non-self-consistent electric field, which produces a pressure peak near dusk during a storm main phase [e.g., *Kozyra et al.*, 1998; *Ebihara and Ejiri*, 2000; *Liemohn et al.*, 2001].

[26] Figure 4 shows the field-aligned current $J_\parallel$, the Pedersen conductance Σ_p, and the convection electric potential Φ for the self-consistent simulation. The field-aligned current is found to flow into the ionosphere mostly in the 0900–1500–2100 MLT region and flows away from the ionosphere mostly in the 2100–0300–0900 MLT region. The conductivity is constant in time for the period shown because Kp was greater than 6 and thus beyond the parameter range of the *Hardy et al.* [1987] model.

[27] In response to space charges deposited in the ionosphere by the field-aligned currents, an additional electric field is produced in the ionosphere. The magnitude of this additional electric field is roughly inversely proportional to the Pedersen conductivity. The bottom panels of Figure 4 show the electric potential in the ionosphere. There are two remarkable regions to be noted.

[28] First, a strong poleward electric field appears in the space between the downward flowing field-aligned current and the auroral oval in the evening sector at 0900 UT (near *Dst* minimum). Since the background conductivity is relatively low equatorward of the auroral oval, a strong poleward electric field is set up in this space. This is most likely associated with the subauroral polarization streams observed at subauroral latitudes [*Foster and Vo*, 2002].

[29] Second, the convection pattern is highly skewed equatorward of the auroral oval in the postmidnight region. This skew is most likely due to the eastward shielding electric field driven by the Region 2 field-aligned current. A flow velocity reversal of the ionospheric plasma observed at subauroral latitudes in the postmidnight region [*Huang et al.*, 2001] may correspond to the deflection of the convection pattern that appears in the bottom panels of Figure 4.

4. Solar EUV Dependence

[30] Figure 5 shows Pedersen conductances for different values of F10.7, indicating obviously that the conductance increases with increasing F10.7. The conductance for F10.7 = 250 $\times$ 10^4 Jy (solar maximum condition) is always higher than for F10.7 = 70 $\times$ 10^4 Jy (solar minimum condition) by a factor of 3 and more.

[31] Figure 6 shows the calculated *Dst** at a fixed time of 0900 UT on 12 August 2000 when *Dst** reached its minimum during the storm, as a function of F10.7. *Dst** is shown to decrease almost linearly with F10.7. The conductance for F10.7 = 250 $\times$ 10^4 Jy results in a 29% stronger ring current than for F10.7 = 70 $\times$ 10^4 Jy.

[32] We used F10.7 to drive the ionospheric and thermospheric models, which govern the modeled conductance.

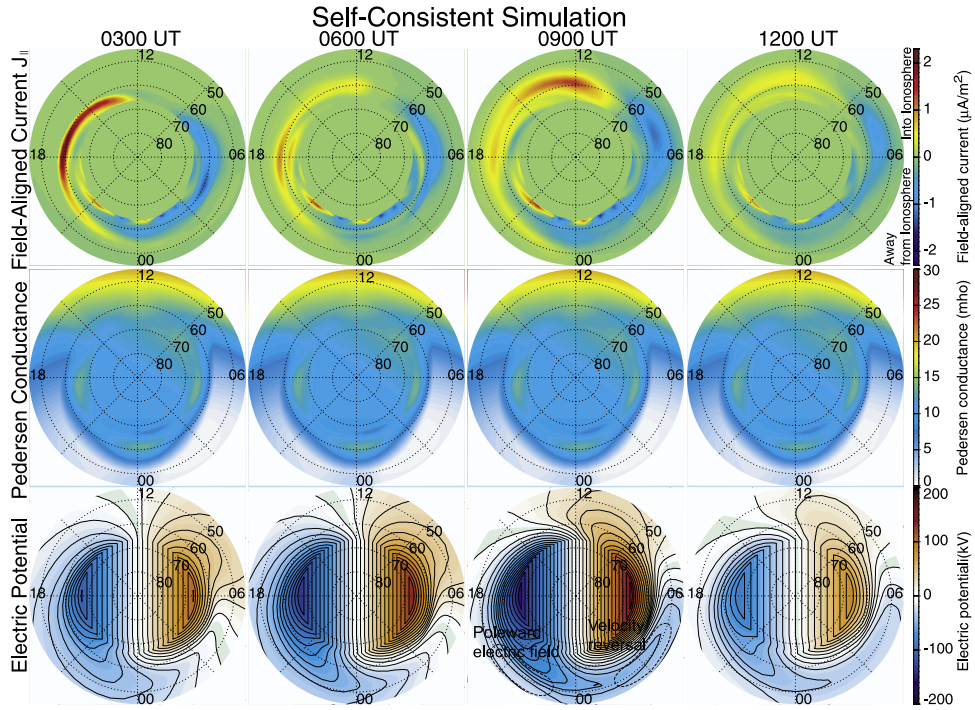

Figure 4. (top) Field-aligned current ($J_{\parallel}$), (middle) half of the two-hemisphere Pedersen conductivity (Σ_P), and (bottom) the electric potential (Φ) in the ionosphere at 100 km altitude in MLT and magnetic latitude coordinates.

F10.7 is known to correspond well with the solar EUV radiation over an 11-year solar-driven cycle [*Hedin*, 1983], and therefore this can cause an 11-year solar cycle in global ionospheric conductivity. Under similar IMF and solar wind conditions, the ring current at the solar maximum should be stronger than at the solar minimum.

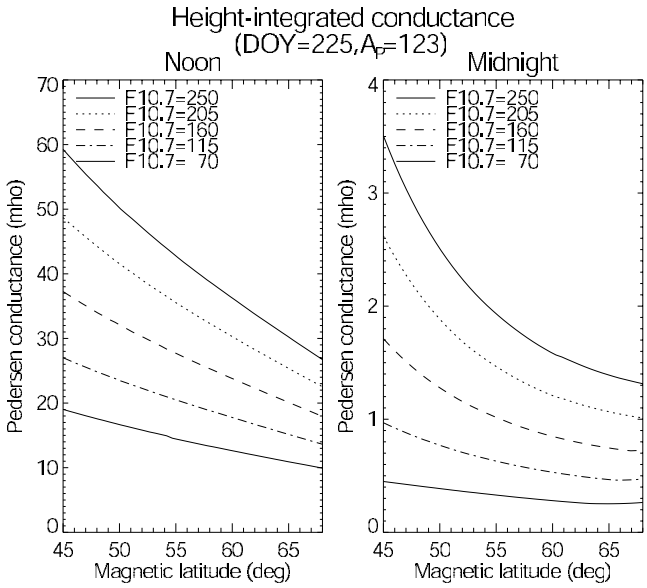

Figure 5. Half intensity of the two-hemisphere Pedersen conductance for different F10.7 values at noon (left) and midnight (right) on day of year (DOY) 205 (12 August). The auroral conductance is excluded. The Ap value was kept constant at 123.

[33] We need to keep in mind that the solar wind and IMF show a solar cycle dependence as well [e.g., *Osherovich et al.*, 1999]. Therefore both the solar cycle variation of the solar wind and IMF and the solar cycle variation of the ionospheric conductivity must contribute to the solar cycle variation of the ring current.

[34] The ionospheric electron density (conductivity) can be enhanced by a sudden enhancement of solar EUV

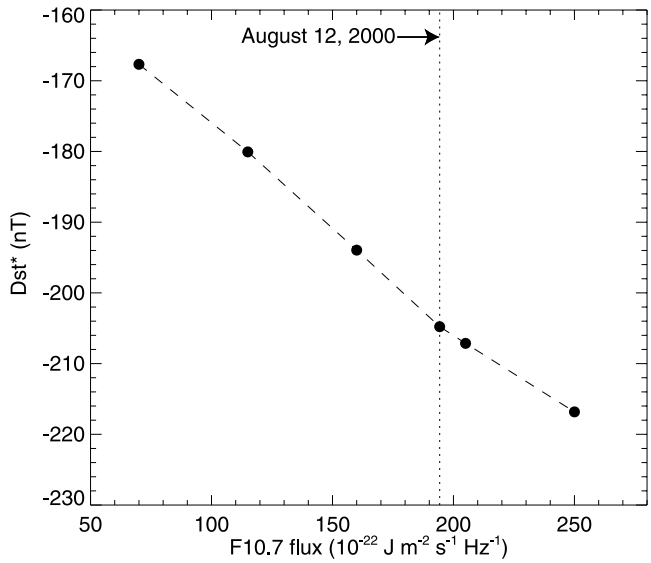

Figure 6. Simulated *Dst** value as a function of F10.7. All other storm conditions were kept fixed. The *Dst** value was taken at the time of 0900 UT on 12 August 2000 when *Dst** reached its minimum during the storm.

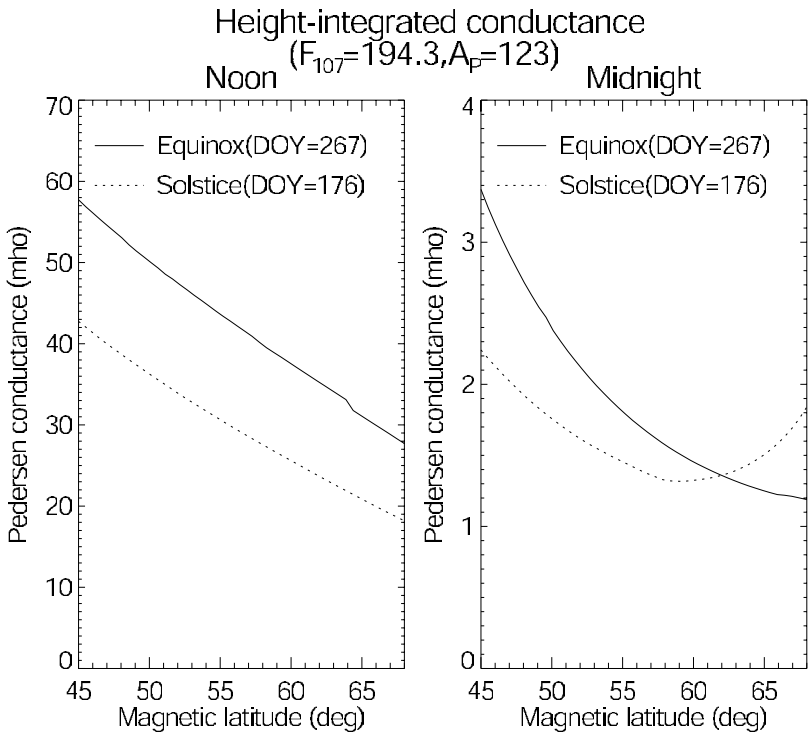

Figure 7. Half intensity of the two-hemisphere Pedersen conductance at equinox (23 September; day of year 267) and the solstice time (24 June; day of year 176) at noon (left) and midnight (right). The auroral conductance is excluded. The Ap and F10.7 values were kept constant at 123. and 194.3, respectively.

radiation during solar flare events [e.g., *Garriott et al.*, 1967, 1969; *Mendillo and Evans*, 1974]. The immediate enhancement of the ionospheric electrons due to a solar flare is called a sudden ionospheric disturbance (SID). An SID should decrease the dayside shielding electric field and may contribute to somewhat the ring current development. We will investigate the influence of SIDs on the ring current in the future.

5. Tilt Angle Dependence

[35] Neutral atoms and molecules above ~60 km are effectively ionized by solar EUV radiation. The degree of the ionization depends largely on the solar zenith angle. Figure 7 shows Pedersen conductances at equinox and solstice. Except for higher latitudes (>62°) at midnight, the Pedersen conductance at equinox is higher than at solstice. At higher latitudes (>62°), the solar zenith angle in the summer hemisphere remains lower than at equinox on the nightside, and thus the lower solar zenith angle produces higher conductivities compared with equinox. Since all parts of the convection electric field are necessarily involved in creating the ring current, a numerical simulation has to be performed to understand the overall effect of the seasonal variation of the conductivity on the ring current.

[36] Figure 8 shows the calculated *Dst** at a fixed time of 0900 UT on 12 August 2000 as a function of the tilt angle in terms of day of year. The result indicates an obvious semiannual variation in that the conductivity at equinox results in about 5% stronger ring current than at solstice.

[37] Figure 9 shows *Dst* averaged over months during the period between 1964 and 2002, indicating clearly a semiannual variation on the average. The ring current at equinox (March and September) is obviously stronger than at solstice (June and December). *Cliver et al.* [2001] also found this effect.

[38] The semiannual variation of the geomagnetic activity has been known for several decades [e.g., *Russell and*

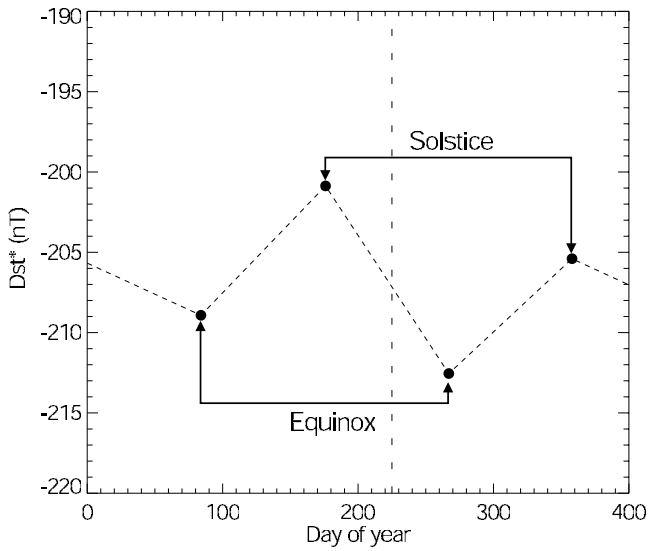

Figure 8. Simulated *Dst** as a function of the tilt angle in terms of day of year. All other storm conditions were kept fixed. The *Dst** value was taken at the time of 0900 UT on 12 August 2000 when *Dst** reached its minimum during the storm.

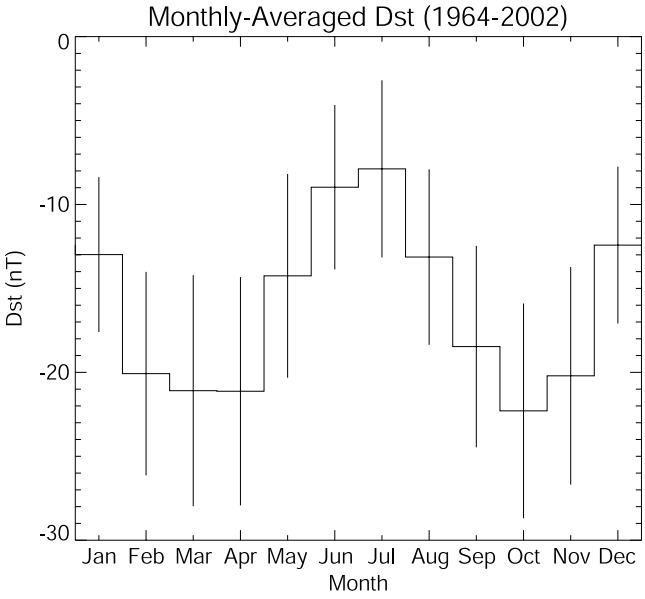

Figure 9. Observed *Dst* averaged over each month. A vertical bar stands for 0.5σ.

McPherron, 1973; *Mayaud*, 1978, 1980; *Crooker and Siscoe*, 1986; *Crooker et al.*, 1992; *Cliver et al.*, 2000, 2001], and four mechanisms have been proposed to account for the semiannual variation [*Cliver et al.*, 2001, and references therein]: (1) the axial hypothesis in which the heliographic latitude of the Earth plays a role, (2) the equinoctial hypothesis in which the orientation of the Earth's axis of rotation relative to the solar equatorial plane plays a role, (3) the IMF effect in which the interaction with the southward component of IMF ordered in solar magnetospheric coordinates (GSM) plays a role, and (4) annual motion of the ring, tail and magnetopause currents with respect to the Earth's magnetic equator.

[39] *Russell and McPherron* [1973] proposed that it is caused by a semiannual variation in the effective southward component of the IMF. *Cliver et al.* [2000] argued that the bulk of the semiannual variation results from the equinoctial effect that makes the IMF coupling less effective at solstice.

[40] Based upon a statistical study, *Cliver et al.* [2001] showed that *Dst* exhibits a semiannual variation with a peak-to-peak amplitude of 10.6 nT. They found that the overall semiannual variation (peak-to-peak amplitude of 10.6 nT) consists of ∼30–50% (3.2–5.3 nT) of the storm component and ∼70–50% (7.4–5.3 nT) of the nonstorm component. As for the storm component, the equinoctial effect accounts for ∼20–40% of the storm component of the semiannual variation while the axial and the IMF effect accounts for 10% of it. As for the nonstorm component of the semiannual variation, a semiannual variation of the ring, tail, and magnetopause currents relative to ground-based magnetometers used for the *Dst* determination is effective [*Fukushima and Nagata*, 1968; *Malin and Isikara*, 1976].

[41] The previously suggested mechanisms involve (1) annual motion of the Earth with respect to the solar equator, (2) the solar wind, (3) IMF, and (4) annual motion of the ring, tail, and magnetopause currents. Our result shown in Figure 8 would lead us to add a new mechanism that involves the semiannual variation of the hemispheric ionospheric conductivity. It is not easy to compare this idea with the observational result derived by a statistical study because an instantaneous picture of the ring current is basically different from a statistical picture of it. Furthermore, the same changes in the solar wind and IMF never appear in the past and in the future, and hence from an observational point of view, we cannot isolate the influence of the conductivity from others without a significant statistical analysis. However, we do expect that the semiannual variation of the hemispheric conductivity in the ionosphere can result in a semiannual variation of *Dst* with a peak-to-peak amplitude of about 5% near the *Dst* minimum for the particular changes in the solar wind and IMF as observed on 12 August 2000.

6. Auroral Conductivity Dependence

[42] The conductance at the latitude of the auroral oval is significant in the ring current development. This can be demonstrated by changing the two-hemisphere height-integrated conductivity associated with auroral electron precipitation. Figure 10 shows calculated *Dst** as a function of magnitude of expansion of the auroral oval compared against the reference auroral conductivity provided by the *Hardy et al.* [1987] model. A positive (negative) value means the auroral oval is being expanded (contracted). The shape and the intensity of the auroral conductivity were kept the same. A minimum value of *Dst** (or the strongest ring current) is achieved when the auroral oval is expanded by 1 or 2deg with respect to the original latitude of the *Hardy et al.* [1987] model for this particular storm. Both the contraction and expansion of the auroral oval from the optimum latitude cause the ring current to be weaker.

[43] Figure 11 shows the conductivity, the field-aligned current, and the plasma pressure in cases of contraction of the auroral oval (by 3deg in magnetic latitude) or expansion

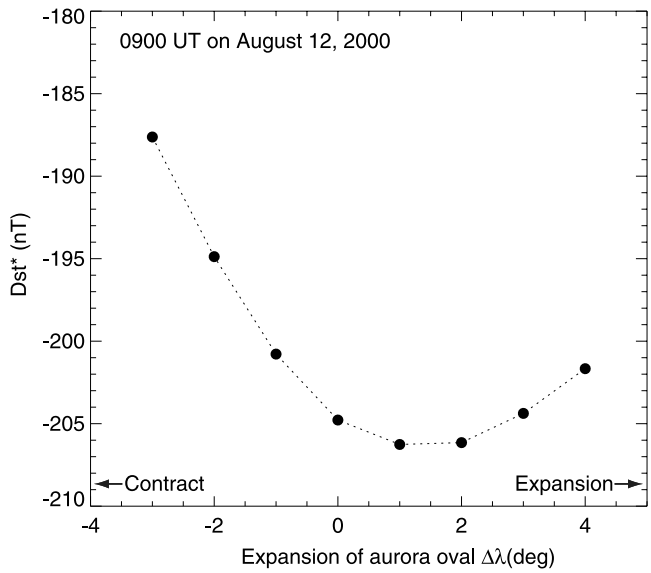

Figure 10. Simulated *Dst** as a function of offset latitude of the auroral conductance. All other storm conditions were kept fixed. The *Dst** value was taken at the time of 0900 UT on 12 August 2000 when *Dst** reached its minimum during the storm.

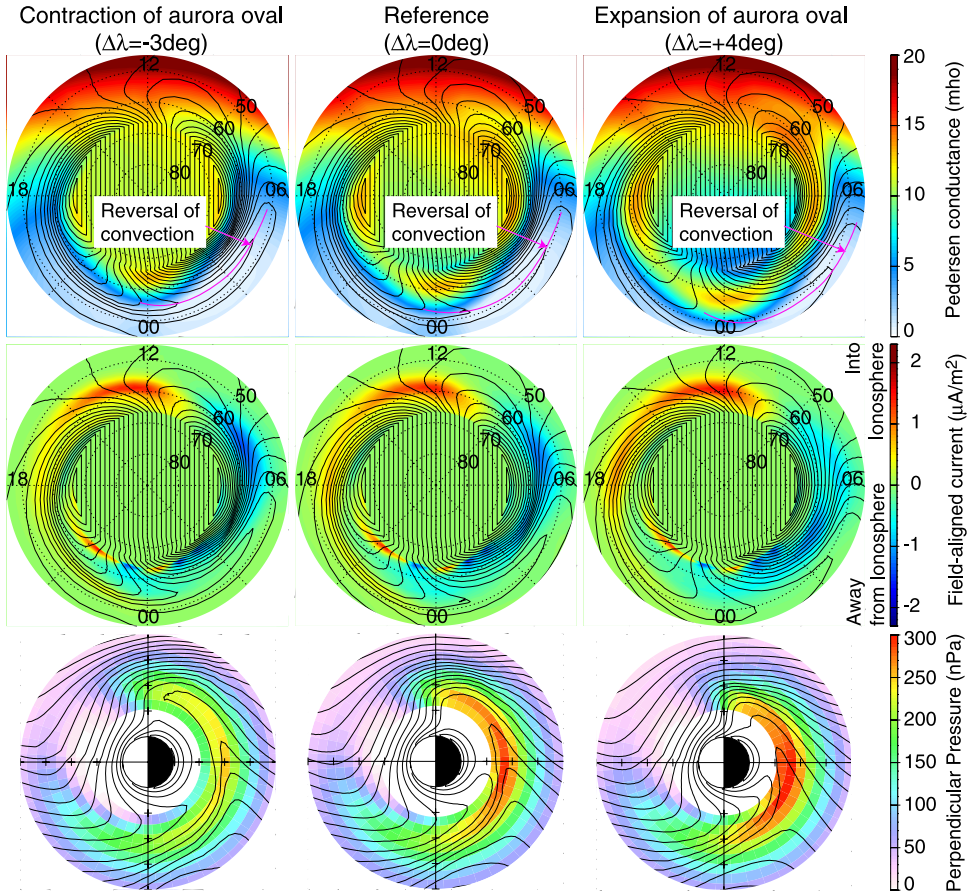

Figure 11. (top) Pedersen conductance, (middle) field-aligned currents in the ionosphere at 100 km altitude, and (bottom) perpendicular plasma pressure in the equatorial plane at 0900 UT on 12 August 2000. The left panels are those in case of contraction of the aurora oval by 3, and the right ones are those in case of expansion of the aurora oval by 4. Electric potential in the corotation frame of reference is overlayed on the first two panels from top. Electric potential in the inertial frame of reference is overlayed on the bottom panels.

of the auroral oval (by 4deg in magnetic latitude). In case of contraction ($\Delta\lambda = -3$deg; left panels), the perpendicular pressure appears weaker and the peak of the pressure occurs farther from the Earth ($L = 3.0$ at midnight) as compared with computations based on the reference conductivity model ($\Delta\lambda = 0$; middle panels). This is reasonably explained by the following mechanism. As the auroral oval is contracted, the reversal of convection in the ionosphere in the postmidnight region shifts poleward because the strong eastward electric field driven by the Region 2 field-aligned current tends to appear just equatorward of the auroral oval. A plasma sheet ion drifting earthward experiences a deflection of the direction of the $\mathbf{E} \times \mathbf{B}$ drift velocity from earthward to westward when the ion intersects the reversal of the convection in the midnight-dawn sector. After intersecting the reversal of the convection, the $\mathbf{E} \times \mathbf{B}$ drift speed becomes slow. This is approximately the innermost limit of the earthward penetration of the plasma sheet particles. Consequently, the peak of the pressure occurs in the vicinity of the inner edge of the plasma sheet, that is, the reversal of the convection in the postmidnight region.

[44] In case of expansion of the auroral oval ($\Delta\lambda = 4$deg; right panels), it is clearly seen that the radial distance of the convection reversal shifts earthward ($L = 2.3$ at midnight). Particles starting in the nightside plasma sheet are adiabatically accelerated by the $\mathbf{E} \times \mathbf{B}$ drift. Before reaching the reversal of the convection ($L = 2.3$ at midnight), the particles gain kinetic energy and then tend to drift westward due to the grad-B and curvature drifts. This limits the inward penetration of the plasma sheet particles. Consequently, the pressure tends to be weak in the morningside when the auroral oval is extremely expanded. When the auroral oval is expanded by 4deg, the perpendicular pressure slightly increases from 290 nPa to 295 nPa at $L = 2.7$ at midnight. However, there is a substantial reduction in the perpendicular pressure from 220 nPa to 130 nPa at $L = 2.7$ at 0600 MLT, and then the total energy decreases.

[45] Since the empirical auroral conductance model given by *Hardy et al.* [1987] is a function of Kp, the model hardly describes short-term and fine-scale variations of conductivity. For example, an auroral breakup typically lasts tens of minutes, while Kp has a resolution of 3 hours. A far ultraviolet imager (FUV) aboard the IMAGE satellite [*Mende et al.*, 2000a, 2000b] is capable of providing an estimate of the auroral conductances with a high temporal resolution of 2 min. Estimating average energy and energy

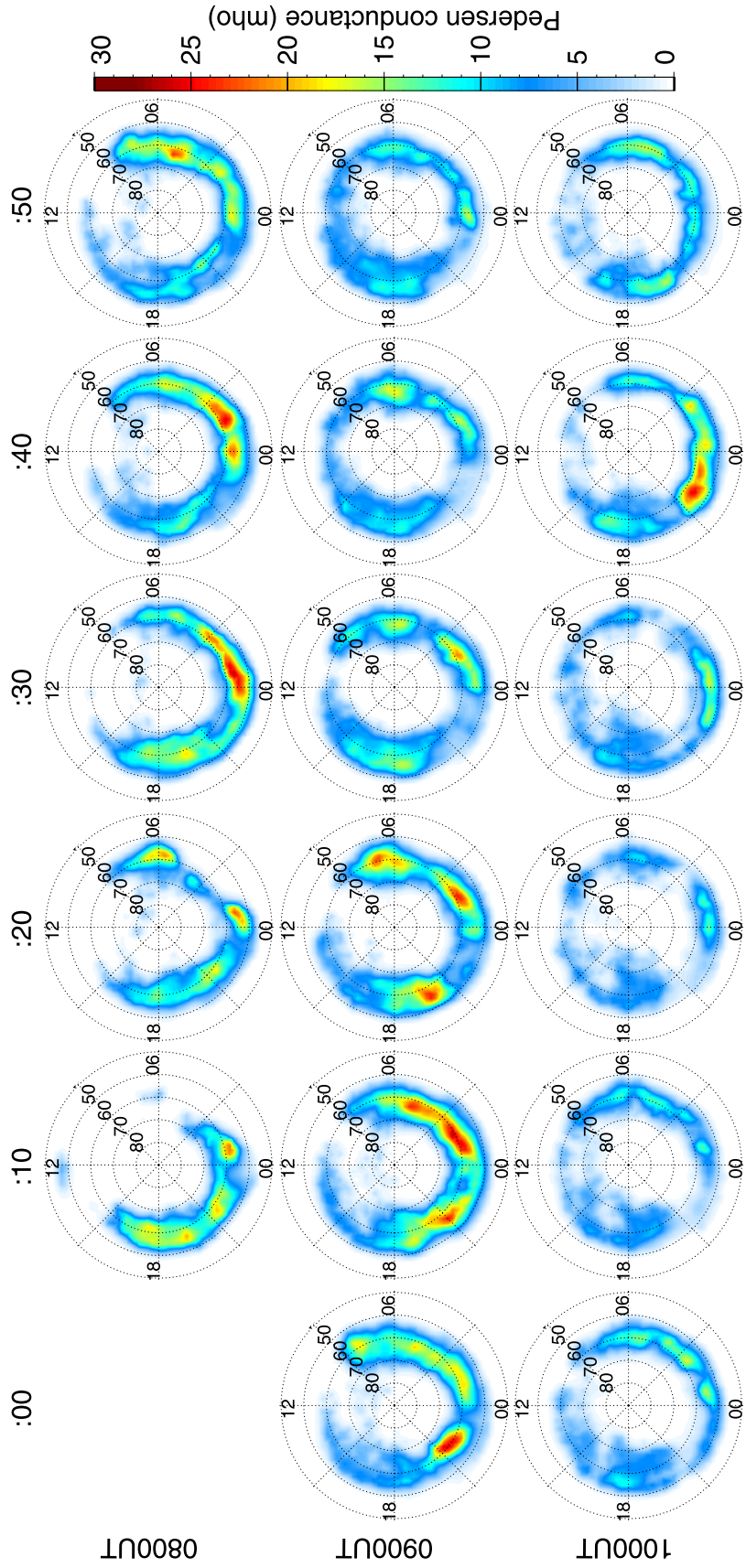

Figure 12. Pedersen conductances estimated from IMAGE/FUV data at 10 min interval between 0810 UT and 1050 UT on 12 August 2000. Snapshots at 2 min interval were used for the simulation. The Pedersen conductances are plotted in the MLT and the magnetic latitude coordinates.

flux of precipitating electrons [*Hubert et al.*, 2002; *Frey et al.*, 2003], Pedersen and Hall conductances can be calculated by using an empirical formula proposed by *Reiff* [1984] as

$$\Sigma_P = F^{1/2}\frac{26\langle E\rangle + 40\langle E\rangle^2 + \langle E\rangle^3}{44 + 1.3\langle E\rangle^3} \tag{16}$$

and

$$\Sigma_H/\Sigma_P = \begin{cases} 0.10, & \text{for} \langle E\rangle < 0.6 \\ -0.04 + 0.2416\langle E\rangle - 0.0022\langle E\rangle^2, & \text{for} \langle E\rangle \geq 0.6 \end{cases} \tag{17}$$

where F is the energy flux in erg cm^{-2} s^{-1} and $\langle E\rangle$ is the average energy in erg.

[46] Original auroral images taken by IMAGE/FUV were accompanied by small-scale fluctuations in space because of insufficient statistics. To remove the highly fluctuating component from the original image, we employed a fast Fourier transform (FFT) filter. The original image was converted from real space to frequency space. After applying a low pass filter to remove the highly fluctuating component, we eventually obtained a smooth image by converting back from frequency space to the real space.

[47] Figure 12 shows snapshots of the Pedersen conductances calculated in the manner described above. Unfortunately, IMAGE/FUV did not take images during the entire period of the storm. We switched the conductance model from the statistical one [*Hardy et al.*, 1987] to the realistic one at 0810 UT when the image of the FUV camera started to cover the whole region of interest, that is, magnetic latitude of 50° and more. After that, we updated the auroral conductance every 2 min. Figure 13 shows the auroral Pedersen conductivity accumulated in the region between 50deg and 60deg in the magnetic latitude. There are four noticeable enhancements of the accumulated Pedersen conductivity due to the auroral electrons, and they peak at 0834, 0911, 0921, and 1039 UT, respectively.

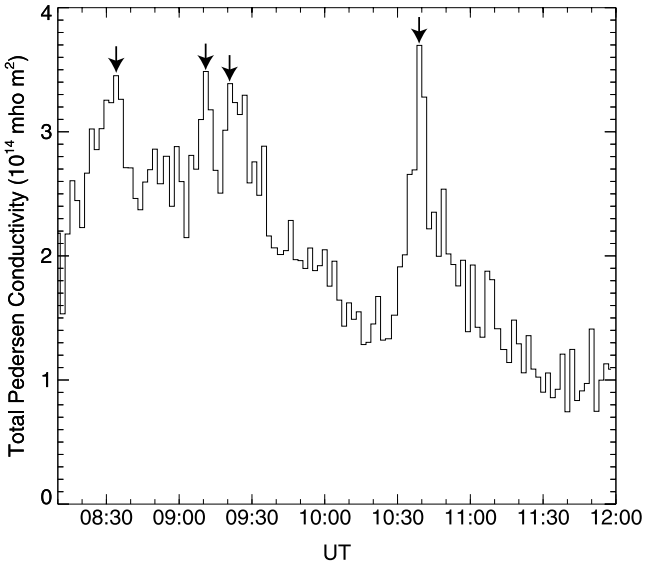

Figure 13. Total Pedersen conductivity due to auroral electron precipitation estimated from IMAGE/FUV data between 50deg and 60deg in the magnetic latitude. Noticeable peaks of the total conductivity are found at 0834, 0911, 0921, and 1039 UT and are indicated with arrows.

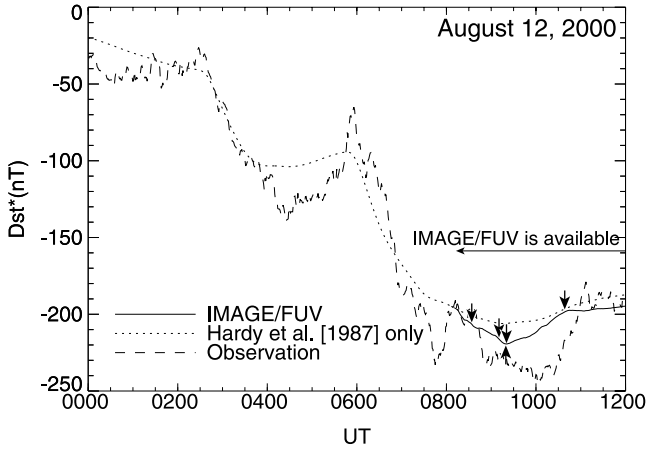

Figure 14. Simulated *Dst** with auroral conductance estimated from IMAGE/FUV (solid line) and the conductance model of *Hardy et al.* [1987] (dashed line). The 1-min SYM index corrected by the solar wind dynamic pressure, as a proxy of *Dst**, is overlayed. An upward arrow stands for a sudden recovery of the ring current, and a downward arrow stands for a peak of the auroral brightening identified in Figure 9.

[48] The *Dst** values calculated with the auroral conductance given by IMAGE/FUV are shown in Figure 14. The 1-min SYM index corrected by the solar wind dynamic pressure is calculated by

$$\text{SYM*} = \text{SYM} - c_1 P_{sw}^{1/2} + c_2 \tag{18}$$

and is overlayed as a proxy of *Dst**. The coefficients c_1 and c_2 are the same as those mentioned in section 2.2. The calculated *Dst** shows a good agreement with the observed one as a zeroth order approximation, and the realistic ionospheric conductivity estimated from the IMAGE/FUV auroral imager data results in about 8% stronger ring current than the empirical conductance model.

[49] Some ambiguities make it difficult to discuss a quantitative comparison between the calculated *Dst** and the observed one. A surface term in the Dessler-Parker-Sckopke relationship is excluded in the calculation. Contributions from other current systems, for example, field-aligned currents and ionospheric currents, may be included in the observed *Dst**. Regarding the variation of the calculated *Dst**, there are three interesting features to be noted.

6.1. First Two Increases in Auroral Activity (0834 and 0911 UT)

[50] The first two auroral activities, peaking at 0834 and 0911 UT, do not modify the *Dst** variation significantly. The auroral brightenings last for 10–20 min, much shorter than the timescale of the storm-time variation of *Dst**.

6.2. Third Increase in Auroral Activity (0921 UT)

[51] In spite of the occurrence of the third increase in auroral activity (peaking at 0921 UT), a rapid recovery of

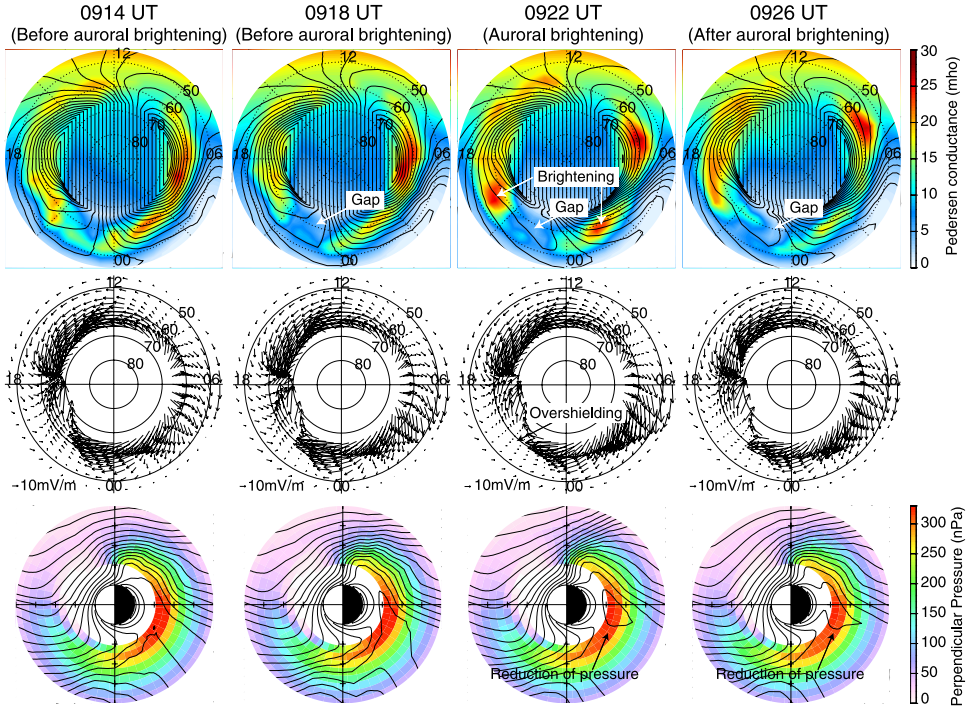

Figure 15. (top) Pedersen conductivity in the ionosphere, (middle) electric field in the corotation frame of reference in the ionosphere, and (bottom) perpendicular pressure in the equatorial plane between 0914 UT (before the noticeable auroral brightening) and 0926 UT (after the brightening). Electric potential in the corotation frame of reference is overlayed on the top panels, and that in the inertial frame of reference is on the bottom panels.

*Dst** starts at 0918 UT (indicated with an upward arrow in Figure 14) and lasts for about 1 hour. This rapid recovery is not obviously caused by decrease in the polar cap potential drop because the polar cap potential drop remains fairly stable around 0918 UT as shown in Figure 2. Figure 15 shows sequential snapshots of the Pedersen conductivity, the ionospheric electric field, and the perpendicular pressure of the ring current protons. At 0918 UT, just prior to the third increase in auroral activity, the auroral oval starts showing morphologically a gap in the region between 2100 and 2300 MLT, and the gap lasts for about 1 hour.

[52] Within the gap, the westward component of the calculated ionospheric electric field becomes weak due to the shielding electric field driven by the Region 2 field-aligned current, and eventually, eastward electric field appears in that particular region as time proceeds. The eastward electric field on the nightside produces the anti-sunward $\mathbf{E} \times \mathbf{B}$ drift velocity that pulls the magnetospheric particles out from small L to large L. As a consequence, the plasma pressure that centers near midnight or premidnight (the bottom panel of Figure 15) decreases rapidly while the gap persists. The perpendicular pressure at $L = 2.6$ at 2200 MLT is 321, 322, 316, and 311 nPa at 0914, 0918, 0922, and 0926 UT, respectively.

[53] The reversed electric field is called the ''overshielded'' electric field because the shielding electric field fed by the Region 2 field-aligned current is strong enough to cancel the electric field directly penetrating from the polar cap [e.g., *Kelley et al.*, 1979; *Spiro et al.*, 1988; *Fejer et al.*, 1990]. The overshielding electric field has been modeled and attributed to a decrease in the polar cap potential drop or the northward turning of IMF [e.g., *Spiro et al.*, 1988; *Peymirat et al.*, 2000]. Since the polar cap potential drop remains almost steady for this particular period of interest, the sudden decrease in the Pedersen conductivity, as morphologically seen by the gap, is understood to produce the overshielding condition leading to the rapid recovery of the ring current.

[54] The third increase in auroral activity that occurred at 0921 UT does not fill the gap as shown in Figure 15. The overshielding persists throughout this interval, and the ring current continues to decrease, regardless of the auroral activity.

[55] The morphological feature of the nightside auroral gap was reported by *Chua et al.* [1998], who showed images captured by the Ultraviolet Imager (UVI) aboard the Polar spacecraft. They suggested that the nightside auroral gap may be due to a significant reduction in field-aligned currents along with an insufficient ionospheric potential to accelerate precipitating electrons within the gap region. A substantial decrease in the plasma pressure, which may generate relevant field-aligned currents within the gap, may maintain the auroral gap if the auroral gap is tightly coupled with the magnetospheric plasma and is associated with a reduction of the intensity of the field-aligned current. The physical mechanism producing the gap is an interesting topic for study but is beyond the scope of this paper.

6.3. Fourth Increase in Auroral Activity (1039 UT)

[56] Regardless of the continuous decay of the polar cap potential drop, the recovery of the ring current is impeded around 1039–1041 UT. This is simply understood to be led

by the weakened shielding electric field associated with the fourth increase in auroral activity that peaks at 1039 UT. The fourth auroral activity fills the gap that appeared 0918 UT as shown in Figure 12, causing reduction of the shielding electric field in the premidnight region where the fourth auroral activity fills the gap.

7. Conclusion

[57] We simulated the particular storm occurred on 12 August 2000. By changing the ionosphere conductivity artificially, we obtained the results that the storm-time ring current is significantly influenced by not only IMF and the solar wind but the solar radiation and the auroral activities as well. The primary results are as follows: (1) The conductivity for solar maximum condition ($F10.7 = 250 \times 10^4$ Jy) results in about 29% stronger ring current than for solar minimum condition ($F10.7 = 70 \times 10^4$ Jy). (2) The conductivity at equinox results in about 5% stronger ring current than at solstice. The semiannual variation of the hemispheric conductivity in the ionosphere would be a new mechanism to explain the semiannual variation of *Dst*. (3) Both expansion and contraction of the auroral oval from an optimal latitude weaken the ring current. (4) The IMAGE/FUV-based conductivity results in about 8% stronger ring current than with the empirical conductance model. (5) The nightside auroral gap that appears at 0918 UT results in the rapid recovery of the ring current for about 1 hour when the gap persists. We showed that a morphological feature of the auroral oval significantly affects the storm-time ring current. Use of realistic auroral conductivities obtained from a satellite-borne auroral imager in numerical simulations may eventually provide much improved understanding of the storm-time ring current and related electrodynamics.

[58] **Acknowledgments.** Grateful acknowledgment is due to Robert W. Spiro for generous support. The computer programs to calculate ionospheric conductivities and solve for the electrostatic potential were written by Stanislav Y. Sazykin as part of his dissertation research at Utah State University. The authors thank S. B. Mende for providing the IMAGE/FUV data and N. F. Ness and D. J. McComas for the ACE data. *Dst* and SYM indices were provided from the World Data Center for Geomagnetism, Kyoto. Y.E. wishes to express his gratitude to Stephen P. Christon, Nat Gopalswamy, and Vladimir A. Osherovich for fruitful comments. This work was supported by the NASA office of Space Science Sun-Earth Connection Guest Investigator Program under RTOP grant 370-16-00-11.

[59] Arthur Richmond thanks Ioannis Daglis and Christophe Peymirat for their assistance in evaluating this paper.

References

Bilitza, D. (1997), International reference ionosphere—Status, 1995/96, *Adv. Space Res.*, *20*, 1751.

Boyle, C. B., P. H. Reiff, and M. R. Hairston (1997), Empirical polar cap potentials, *J. Geophys. Res.*, *102*, 111–125.

Chen, M. W., M. Schulz, L. R. Lyons, and D. J. Gorney (1993), Stormtime transport of ring current and radiation belt ions, *J. Geophys. Res.*, *98*, 3835.

Christon, S. P., U. Mall, T. E. Eastman, G. Gloeckler, A. T. Y. Lui, R. W. McEntire, and E. C. Roelof (2002), Solar cycle and geomagnetic N+1/O+1 variation in outer dayside magnetosphere: Possible relation to topside ionosphere, *Geophys. Res. Lett.*, *29*(5), 1058, doi:10.1029/2001GL013988.

Chua, D., M. Brittnacher, G. Parks, G. Germany, and J. Spann (1998), A new auroral feature: The nightside gap, *Geophys. Res. Lett.*, *25*, 3747.

Cliver, E. W., Y. Kamide, and A. G. Ling (2000), Mountains versus valleys: The semiannual variation of geomagnetic activity, *J. Geophys. Res.*, *105*, 2413.

Cliver, E. W., Y. Kamide, A. G. Ling, and N. Yokoyama (2001), Semiannual variation of the geomagnetic *Dst* index: Evidence for a dominant nonstorm component, *J. Geophys. Res.*, *106*, 21,297.

Crooker, N. U., and G. L. Siscoe (1986), The effect of the solar wind on the terrestrial environment, in *Physics of the Sun*, edited by P. A. Sturrock, p. 193, D. Reidel, Norwell, Mass.

Crooker, N. U., E. W. Cliver, and B. T. Tsurutani (1992), The semiannual variation of great geomagnetic storms and the postshock Russell-McPherron effect preceding coronal mass ejecta, *Geophys. Res. Lett.*, *19*, 429.

C:son Brandt, P., S. Ohtani, D. G. Mitchell, M.-C. Fok, E. C. Roelof, and R. Demajistre (2002), Global ENA observations of the storm mainphase ring current: Implications for skewed electric fields in the inner magnetosphere, *Geophys. Res. Lett.*, *29*(20), 1954, doi:10.1029/2002GL015160.

Daglis, I. A. (1997), The role of magnetosphere-ionosphere coupling in magnetic storm dynamics, in *Magnetic Storms*, *Geophys. Monogr. Ser.*, vol. 98, edited by B. T. Tsurutani et al., pp. 107–116, AGU, Washington, D. C.

Dessler, A. J., and E. N. Parker (1959), Hydrodynamic theory of geomagnetic storms, *J. Geophys. Res.*, *64*, 2239.

Ebihara, Y., and M. Ejiri (1998), Modeling of solar wind control of the ring current buildup: A case study of the magnetic storms in April 1997, *Geophys. Res. Lett.*, *25*, 3751.

Ebihara, Y., and M. Ejiri (2000), Simulation study on fundamental properties of the storm-time ring current, *J. Geophys. Res.*, *105*, 15,843.

Ebihara, Y., and M. Ejiri (2003), Numerical simulation of the ring current: Review, *Space Sci. Rev.*, *105*, 377.

Ebihara, Y., M. Ejiri, H. Nilsson, I. Sandahl, A. Milillo, M. Grande, J. F. Fennell, and J. L. Roeder (2002), Statistical distribution of the storm-time proton ring current: POLAR measurements, *Geophys. Res. Lett.*, *29*(20), 1969, doi:10.1029/2002GL015430.

Fejer, B. G., R. W. Spiro, R. A. Wolf, and J. C. Foster (1990), Latitudinal variation of perturbation electric fields during magnetically disturbed periods: 1986 SUNDIAL observations and model results, *Ann. Geophys.*, *8*, 441.

Fok, M.-C., and T. E. Moore (1997), Ring current modeling in a realistic magnetic field configuration, *Geophys. Res. Lett.*, *24*, 1775.

Fok, M.-C., T. E. Moore, J. U. Kozyra, G. C. Ho, and D. C. Hamilton (1995), Three-dimensional ring current decay model, *J. Geophys. Res.*, *100*, 9619.

Fok, M.-C., R. A. Wolf, R. W. Spiro, and T. E. Moore (2001), Comprehensive computational model of Earth's ring current, *J. Geophys. Res.*, *106*, 8417.

Fok, M. C., et al. (2003), Global ENA image simulations, *Space Sci. Rev.*, *109*, 77.

Foster, J. C., and H. B. Vo (2002), Average characteristics and activity dependence of the subauroral polarization stream, *J. Geophys. Res.*, *107*(A12), 1475, doi:10.1029/2002JA009409.

Frey, H. U., T. J. Immel, S. B. Mende, J.-C. Gérard, B. Hubert, S. Habraken, J. Spann, G. R. Gladstone, D. V. Bisikalo, and V. I. Shematouth (2003), Summary of quantitative interpretation of IMAGE far ultraviolet aurorae data, *Space Sci. Rev.*, *109*, 255.

Fukushima, N., and T. Nagata (1968), Morphology of magnetic disturbance, *Ann. Geophys.*, *24*, 583.

Garriott, O. K., A. V. da Rosa, M. J. Davis, and D. G. Villard Jr. (1967), Solar flare effects in the ionosphere, *J. Geophys. Res.*, *72*, 6099.

Garriott, O. K., A. V. da Rosa, L. A. Wagner, and G. D. Thome (1969), Enhancement of ionizing radiation during a solar flare, *Sol. Phys.*, *8*, 226.

Gloeckler, G., B. Wilken, W. Studemann, F. M. Ipavich, D. Hovestadt, D. C. Hamilton, and G. Kremser (1985), First composition measurement of the bulk of the storm-time ring current (1 to 300 keV/e) with AMPTE-CCE, *Geophys. Res. Lett.*, *12*, 325.

Gonzalez, W. D., J. A. Joselyn, Y. Kamide, H. W. Kroehl, G. Rostoker, B. T. Tsurutani, and V. M. Vasyliunas (1994), What is a geomagnetic storm?, *J. Geophys. Res.*, *99*, 5771.

Hamilton, D. C., G. Gloeckler, F. M. Ipavich, W. Studemann, B. Wilken, and G. Kremser (1988), Ring current development during the great geomagnetic storm of February 1986, *J. Geophys. Res.*, *93*, 14,343–14,355.

Hardy, D. A., M. S. Gussenhoven, and E. Holeman (1985), A statistical model of auroral electron precipitation, *J. Geophys. Res.*, *90*, 4229.

Hardy, D. A., M. S. Gussenhoven, R. Raistrick, and W. J. McNeil (1987), Statistical and functional representations of the pattern of auroral energy flux, number flux, and conductivity, *J. Geophys. Res.*, *92*, 12,275–12,294.

Harel, M., R. A. Wolf, P. H. Reiff, R. W. Spiro, W. J. Burke, F. J. Rich, and M. Smiddy (1981a), Quantitative simulation of a magnetospheric substorm: 1. Model logic and overview, *J. Geophys. Res.*, *86*(A4), 2217.

Harel, M., R. A. Wolf, R. W. Spiro, P. H. Reiff, C.-K. Chen, W. J. Burke, F. J. Rich, and M. Smiddy (1981b), Quantitative simulation of a magnetospheric substorm: 2. Comparison with observations, *J. Geophys. Res.*, *86*, 2242.

Hedin, A. E. (1983), A revised thermospheric model based on Mass Spectrometer and Incoherent Scatter data: MSIS-83, *J. Geophys. Res.*, *88*, 10,170.

Hedin, A. E. (1991), Extension of the MSIS thermospheric model into the middle and lower atmosphere, *J. Geophys. Res.*, *96*, 1159.

Huang, C.-S., J. C. Foster, and J. M. Holt (2001), Westward plasma drift in the midlatitude ionospheric F region in the midnight-dawn sector, *J. Geophys. Res.*, *106*, 30,349.

Hubert, B., J.-C. Gérard, D. S. Evans, M. Meurant, S. B. Mende, H. U. Frey, and T. J. Immel (2002), Total electron and proton energy input during auroral substorms: Remote sensing with IMAGE-FUV, *J. Geophys. Res.*, *107*(A8), 1183, doi:10.1029/2001JA009229.

Jaggi, R. K., and R. A. Wolf (1973), Self-consistent calculation of the motion of a sheet of ions in the magnetosphere, *J. Geophys. Res.*, *78*, 2852.

Jordanova, V. K., L. M. Kistler, J. U. Kozyra, G. V. Khazanov, and A. F. Nagy (1996), Collisional losses of ring current ions, *J. Geophys. Res.*, *101*, 111.

Kelley, M. C., B. G. Fejer, and C. A. Gonzales (1979), An explanation for anomalous equatorial ionospheric electric fields associated with a northward turning of the interplanetary magnetic field, *Geophys. Res. Lett.*, *6*, 301.

Khazanov, G. V., M. W. Liemohn, T. S. Newman, M.-C. Fok, and R. W. Spiro (2003), Self-consistent magnetospheric-ionospheric coupling: Theoretical studies, *J. Geophys. Res.*, *108*(A3), 1122, doi:10.1029/2002JA009624.

Kozyra, J. U., V. K. Jordanova, J. E. Borovsky, M. F. Thomsen, D. J. Knipp, D. S. Evans, D. J. McComas, and T. E. Cayton (1998), Effects of a high-density plasma sheet on ring current development during the November 2–6, 1993, magnetic storm, *J. Geophys. Res.*, *103*, 26,285.

Liemohn, M. W., J. U. Kozyra, V. K. Jordanova, G. V. Khazanov, M. F. Thomsen, and T. E. Cayton (1999), Analysis of early phase ring current recovery mechanisms during geomagentic storms, *Geophys. Res. Lett.*, *26*, 2845.

Liemohn, M. W., J. U. Kozyra, M. F. Thomsen, J. L. Roeder, G. Lu, J. E. Borovsky, and T. E. Cayton (2001), Dominant role of the asymmetric ring current in producing the stormtime *Dst**, *J. Geophys. Res.*, *106*, 10,883.

Lundin, R., L. R. Lyons, and N. Pissarenko (1980), Observations of the ring current composition at L < 4, *Geophys. Res. Lett.*, *7*, 425.

Malin, S. R. C., and A. M. Isikara (1976), Annual variation of the geomagnetic field, *Geophys. J. R. Astron. Soc.*, *47*, 445.

Mall, U., S. Christon, E. Kirsch, and G. Gloeckler (2002), On the solar cycle dependence of the N+/O+ content in the magnetosphere and its relation to atomic N and O in the Earth's exosphere, *Geophys. Res. Lett.*, *29*(12), 1593, doi:10.1029/2001GL013957.

Mayaud, P. N. (1978), The annual and daily variations of the *Dst* index, *Geophys. J. R. Astron. Soc.*, *55*, 193.

Mayaud, P. N. (Ed.) (1980), *Derivation, Meaning and Use of Geomagnetic Indices*, *Geophys. Monogr. Ser.*, vol. 22, AGU, Washington, D. C.

Mende, S. B., et al. (2002a), Far ultraviolet imaging from the IMAGE spacecraft: 2. Wideband FUV imaging, *Space Sci. Rev.*, *91*, 271.

Mende, S. B., et al. (2000b), Far ultraviolet imaging from the IMAGE spacecraft. 3. Spectral imaging of Lyman-α and OI 135. 6 nm, *Space Sci. Rev.*, *91*, 287.

Mendillo, M., and J. V. Evans (1974), Incoherent scatter observations of the ionospheric response to a large solar flare, *Radio Sci.*, *9*, 197.

Moore, T. E., and D. C. Delcourt (1995), The geopause, *Rev. Geophys.*, *33*, 175.

Osherovich, V. A., J. Fainberg, and R. G. Stone (1999), Solar wind quasi-invariant as a new index of solar activity, *Geophys. Res. Lett.*, *26*, 2597.

Peymirat, C., A. D. Richmond, and A. T. Kobea (2000), Electrodynamic coupling of high and low latitudes: Simulations of shielding/overshielding effects, *J. Geophys. Res.*, *105*, 22,991.

Reiff, P. H. (1984), Models of auroral-zone conductances, in *Magnetospheric Currents*, *Geophys. Monogr. Ser.*, vol. 28, edited by T. A. Potemra, p. 180, AGU, Washington, D. C.

Ridley, A. J., and M. W. Liemohn (2002), A model-derived storm time asymmetric ring current driven electric field description, *J. Geophys. Res.*, *107*(A8), 1151, doi:10.1029/2001JA000051.

Robinson, R. M., R. R. Vondrak, K. Miller, T. Dabbs, and D. Hardy (1987), On calculating ionospheric conductances from the flux and energy of precipitating electrons, *J. Geophys. Res.*, *92*, 2565–2569.

Roeder, J. L., J. F. Fennell, M. W. Chen, M. Grande, S. Livi, and M. Schulz (1996), CRRES observations of stormtime ring current ion composition, in *Workshop on the Earth's Trapped Particle Environment*, *AIP Conf. Proc.*, 383, 131–135.

Russell, C. T., and R. L. McPherron (1973), Semiannual variation of geomagnetic activity, *J. Geophys. Res.*, *78*, 92.

Sckopke, N. (1966), A generation relation between the energy of trapped particles and the disturbance field near the earth, *J. Geophys. Res.*, *71*, 3125.

Senior, C., and M. Blanc (1984), On the control of magnetospheric convection by the spatial distribution of ionospheric conductivities, *J. Geophys. Res.*, *89*, 261.

Sheldon, R. B., and D. C. Hamilton (1993), Ion transport and loss in the Earth's quiet ring current: 1. Data and standard model, *J. Geophys. Res.*, *98*, 13,491–13,508.

Spiro, R. W., and R. A. Wolf (1984), Electrodynamics of convection in the inner magnetosphere, in *Magnetospheric Currents*, *Geophys. Monogr. Ser.*, vol. 28, edited by T. A. Potemra, p. 248, AGU, Washington, D. C.

Spiro, R. W., M. Harel, R. A. Wolf, and P. H. Reiff (1981), Quantitative simulation of a magnetospheric substorm: 3. Plasmaspheric electric fields and evolution of the plasmapause, *J. Geophys. Res.*, *86*, 2261.

Spiro, R. W., R. A. Wolf, and B. G. Fejer (1988), Penetration of high-latitude-electric-field effects to low latitudes during SUNDIAL 1984, *Ann. Geophys.*, *6*, 39.

Stern, D. P. (1975), The motion of a proton in the equatorial magnetosphere, *J. Geophys. Res.*, *80*, 595.

Toffoletto, F., S. Sazykin, R. Spiro, and R. Wolf (2003), Inner magnetospheric modeling with the Rice Convection Model, *Space Sci. Rev.*, *107*, 175.

Tsyganenko, N. A. (1995), Modeling the Earth's magnetospheric magnetic field confined within a realistic magnetopause, *J. Geophys. Res.*, *100*, 5599.

Tsyganenko, N. A., and D. P. Stern (1996), A new-generation global magnetosphere field model, based on spacecraft magnetometer data, *ISTP Newsl.*, *6*(1), 21.

Vasyliunas, V. M. (1970), Mathematical models of magnetospheric convection and its coupling to the ionosphere, in *Particles and Fields in the Magnetosphere*, edited by B. McCormac, p. 60, D. Reidel, Norwell, Mass.

Volland, H. (1973), A semiempirical model of large-scale magnetospheric electric fields, *J. Geophys. Res.*, *78*, 171.

Weimer, D. R. (1995), Models of high-latitude electric potentials derived with a least error fit of spherical coefficients, *J. Geophys. Res.*, *100*, 19,595.

Weimer, D. R. (2001), An improved model of ionospheric electric potentials including substorm perturbations and application to the Geospace Environment Modeling November 24, 1996, event, *J. Geophys. Res.*, *106*, 407.

Wolf, R. A. (1970), Effects of ionospheric conductivity on convection flow of plasma in the magnetosphere, *J. Geophys. Res.*, *75*, 4677.

Wolf, R. A., R. W. Spiro, G.-H. Voigt, P. H. Reiff, C. K. Chen, and M. Harel (1982), Computer simulation of inner magnetospheric dynamics for the magnetic storm of July 29, 1977, *J. Geophys. Res.*, *87*, 5949.

Y. Ebihara, Universities Space Research Association, NASA Goddard Space Flight Center, Code 692, Greenbelt, MD 20771, USA. (ebihara@lepvax.gsfc.nasa.gov)

M.-C. Fok and T. E. Moore, NASA Goddard Space Flight Center, Code 692, Greenbelt, MD 20771, USA. (mei-ching.h.fok@nasa.gov; thomas.e.moore@nasa.gov)

T. J. Immel, Space Sciences Laboratory, University of California, Berkeley, Berkeley, CA 94720-7450, USA. (immel@ssl.berkeley.edu)

R. A. Wolf, Physics and Astronomy Department, Rice University, MS108, P.O. Box 1892, Houston, TX 77251-1892, USA. (rawolf@rice.edu)